A Robust Data-Driven Framework for Evaluating the Hydraulic Efficiency of Piano Key and Labyrinth Weirs

Afshin Bifan [1], Alireza Yazdani [*,1], Mohammad Heidarnejad [2]

1. Department of Civil Engineering, Na.C., Islamic Azad University, Najafabad, Iran.
2. Department of Water Science Engineering, Ahv.C., Islamic Azad University, Ahvaz, Iran.

ABSTRACT

This study presents a comparative evaluation of three machine learning algorithms- Multivariate Adaptive Regression Splines (MARS), Support Vector Machine (SVM), and Gene Expression Programming (GEP)- for predicting the discharge coefficient (C_d) of labyrinth and piano-key weirs. Experimental data were collected from various linear and arced configurations in a laboratory flume. Dimensional analysis identified four key dimensionless predictors: $\frac{H_T}{P}$, Fr, $\frac{L}{W}$ and $\frac{R}{W}$. The results demonstrated that while all models provided acceptable trends, the optimized MARS architecture exhibited superior statistical performance and stability. In the training phase, MARS achieved an R^2 of 0.9882, RMSE of 0.0194, and MAE of 0.0157, significantly outperforming SVM (R^2=0.864) and GEP (R^2=0.967). The robustness was further confirmed in the testing phase, where MARS maintained a high R^2 of 0.9792 and a $C_{d(DDR)max}$ of 6.6331, indicating minimal stochastic variance. Sensitivity analysis revealed that $\frac{H_T}{P}$ and Fr are the most influential parameters, each referenced six times in the MARS basis functions. Furthermore, the Kernel Density Estimation (KDE) and scatter plots validated the high-fidelity alignment of MARS predictions with experimental observations along the 1:1 identity line. The study concludes that the white-box MARS model, with its explicit governing equations and low GCV error (0.000777), serves as the most reliable and transparent computational tool for estimating the hydraulic capacity of complex non-linear weir systems.

KEYWORDS
Discharge coefficient, Data-Based model, Labyrinth weirs, Piano-key weirs, Predictive modeling.

1. Introduction

Spillways are critical hydraulic structures for ensuring dam safety, and inadequate discharge capacity has historically contributed to a significant proportion of dam failures. To enhance discharge efficiency under limited upstream head and constrained spillway width, nonlinear crest geometries such as labyrinth weirs- and more recently Piano Key (PK) weirs- have been developed to increase the effective crest length within a given footprint [1].

***Corresponding Author:**
Alireza Yazdani

Email: alirezayazdani@iau.ac.ir
Received: 2026.07.01
Accepted: 2026.08.23
J. Hydraul. Struct., 13(1): 45-70
DOI: 10.22055/jhs.2026.52530.1389

These structures are capable of passing large discharges at relatively low heads and are therefore widely applied in dam rehabilitation projects and in situations where structural or topographic constraints limit conventional spillway expansion [2-4]. However, their hydraulic behavior is inherently three-dimensional and strongly influenced by crest geometry, planform configuration, upstream approach conditions, and the head-to-height ratio. Variations in flow regime- from fully aerated to transitional and ultimately suppressed flow- can substantially affect the discharge coefficient, making its accurate prediction complex [5-7]. Owing to this complexity, discharge capacity assessment has traditionally relied on extensive laboratory experimentation and empirical formulations. Despite significant experimental advances, the development of reliable and generalizable predictive models for the discharge coefficient remains a challenge. Accordingly, numerous studies have been conducted by different researchers to simulate and predict the discharge coefficient of nonlinear spillways using experimental, numerical, and data-driven approaches; several representative studies in this field are briefly reviewed below.

Sinha et al. [8] experimentally compared two Type A Piano Key Weirs with different outlet key geometries (linear and curvilinear ogee) under free-flow conditions (H/P = 0.17–0.63). Their results showed that the curvilinear ogee outlet increased discharge efficiency by 12-18% by reducing nappe interference and flow separation. Using 90 datasets, they proposed a new empirical equation for predicting the discharge coefficient, which achieved predictive accuracy comparable to or better than existing formulations. Mirzad and Kouchakzadeh [9] investigated the hydraulic behavior of a Type-A Piano Key Weir under steady and unsteady flow conditions using combined physical experiments and numerical modeling. Eight steady and fifty-three unsteady tests were conducted. Results showed significant differences between steady and unsteady stage–discharge relationships, with errors up to 41%. The Modified Puls method predicted outflow with high accuracy (error <5%), highlighting the importance of considering unsteady flow effects in PKW analysis. Quamar and Ahmad [10] applied machine learning models (SVR, XGBoost, RF, and hybrid SVR–RF) to predict the discharge coefficient of Type-A Piano Key Weirs. SVR achieved the best accuracy (R^2 = 0.9916). SHAP analysis identified relative crest length (L/W) as the most influential parameter, and a GUI was developed for real-time CPKW prediction. Belay et al. [11] experimentally examined downstream void fraction distribution of nonlinear weirs using piano key, labyrinth, and linear weir models. Results showed significant cross-sectional variability in air concentration influenced by plunging jets, standing waves, and tailwater depth. Labyrinth weirs produced higher void fractions than piano key weirs, and a simplified relationship for depth-averaged void fraction was proposed. Hamidinia et al. [12] investigated labyrinth and piano key weirs with and without stepped sidewalls to examine inlet immersion effects. Experiments with six stepped-wall models showed that increasing step height reduced the discharge coefficient by up to 50% in labyrinth weirs and 39% in PKWs. Labyrinth weirs performed better, with higher discharge coefficients and peak values at Fr = 0.94 (LW) and Fr = 0.83 (PKW). Hussein [13] evaluated the hydraulic performance of various weir types under different environmental conditions. Results showed that rectangular weirs provide stable discharge with elevation changes, while trapezoidal labyrinth and piano key weirs exhibited inconsistent or reduced performance with increased height. Stepped labyrinth weirs offered improved stability, and further optimization using computational modeling was recommended. Eltarabily et al. [14] numerically and experimentally investigated hydraulic

performance and energy dissipation of different Piano Key Weir (PKW) types using FLOW-3D. Type-B showed superior discharge at low heads (Ht/P ≤ 0.40), while Type-A performed best at higher heads. Type-C achieved the highest energy dissipation. An empirical equation was proposed to estimate energy dispersion from the discharge coefficient. Majedi-Asl et al. [15] evaluated Support Vector Machine (SVM) and Gene Expression Programming (GEP) models to predict the discharge coefficient (Cd) of piano key, rectangular labyrinth, and trapezoidal labyrinth weirs using experimental data and dimensional analysis. Both models performed well, but GEP outperformed SVM. Sensitivity analysis identified the most influential parameters for each weir type. Singh et al. [16] reviewed the development, geometry, and hydraulic performance of Piano Key Weirs (PKWs) for dam rehabilitation and new projects. Comparing PKWs with rectilinear and nonlinear weirs, they highlighted superior discharge capacity, aeration efficiency, sediment management, and cost-effectiveness. The study concluded that PKWs are effective for dam risk mitigation and identified directions for future research.

Although several machine-learning techniques such as ANN, SVM, GEP, Random Forest, and XGBoost have been applied to estimate the discharge coefficient of labyrinth and piano-key weirs, previous studies have primarily emphasized predictive accuracy, while comparatively little attention has been devoted to developing interpretable data-driven models that simultaneously provide explicit analytical equations and identify nonlinear interactions among hydraulic variables. Among available machine-learning approaches, Multivariate Adaptive Regression Splines (MARS) has received very limited attention in nonlinear weir hydraulics despite its ability to automatically detect breakpoints, model nonlinear interactions, and generate transparent piecewise mathematical relationships suitable for engineering design. Therefore, the main objective of this study is to investigate the capability of MARS for predicting the discharge coefficient of labyrinth and piano-key weirs using experimentally derived dimensionless parameters and to benchmark its performance against two well-established algorithms, namely SVM and GEP. Beyond comparing prediction accuracy, this study aims to develop an interpretable predictive equation and identify the dominant hydraulic variables controlling discharge performance, thereby providing a practical white-box modeling framework for hydraulic engineers.

Materials and methods

Data collection

In the present study, a series of physical experiments were carried out to systematically investigate the parameters affecting the discharge coefficient (C_d) of both labyrinth and piano key weirs. The experimental campaign was conducted in the Hydraulic Laboratory of the Khuzestan Water and Power Authority (KWPA), Iran. All tests were performed in a precision-engineered, glass-walled rectangular flume measuring 8 m in length, 0.6 m in width, and 0.6 m in height, featuring a horizontal slope (S_0=0). Flow was supplied to the flume from a head tank via a closed-loop system driven by a centrifugal pump. To ensure a fully developed, tranquil approach flow and to eliminate macro-turbulence, the inlet section of the flume was equipped with honeycomb flow straighteners and baffle screens. The inflow discharge (Q) was regulated using a high-precision control valve and measured upstream using an electromagnetic flowmeter with an accuracy of ±5%, spanning a discharge range of 5 to 45 L/s. The flow depth and upstream hydraulic head were measured at a distance of 4P (where P is the weir height) upstream of the weir crest to avoid the drawdown curve zone. These measurements were recorded using a digital point gauge with a resolution of ±0.1 mm. To ensure high data quality and check for repeatability, each

experimental run was allowed to reach a steady-state condition (defined by a constant head reading over a 10-minute interval) before data recording. Furthermore, random replicate tests were conducted for 15% of the configurations, showing a maximum discrepancy of less than 1.8% in the calculated C_d. Fig. 1 illustrates the detailed plan view and longitudinal profile of the experimental flume setup.

In the present research, physical models of all weirs were constructed from Plexiglas with a thickness of 3 mm and a crest height of 6 cm. To provide a clearer understanding of the dimensions and design of the weir models, their geometric and hydraulic characteristics are presented in Table 1. Additionally, Figs. 2 and 3 show the plan view and the physical models of the weirs used in the experiments, respectively. The geometric configurations of the tested weir models are schematically illustrated in Figure 4. The right panel displays the arced-labyrinth weir, which is defined by its cycle geometry, including the apex angle (α), the wall thickness (t_w), and the side wall length (l_c). The overall layout of the arced weir is characterized by the radius (R) and the central angle (θ) relative to the channel width (W). The left panel presents the piano-key weir (PKW) model. This includes a plan view showing the arrangement of inlet and outlet keys with a base length (B). To illustrate the internal sloped floor of the PKW, two longitudinal cross-sections are provided: section A-A representing the outlet key and section B-B representing the inlet key.

Table 1 provides a comprehensive summary of the geometric and hydraulic characteristics of the various non-linear weirs investigated in the present study. This table details the dimensions of both linear and arced configurations for labyrinth and piano-key weirs.

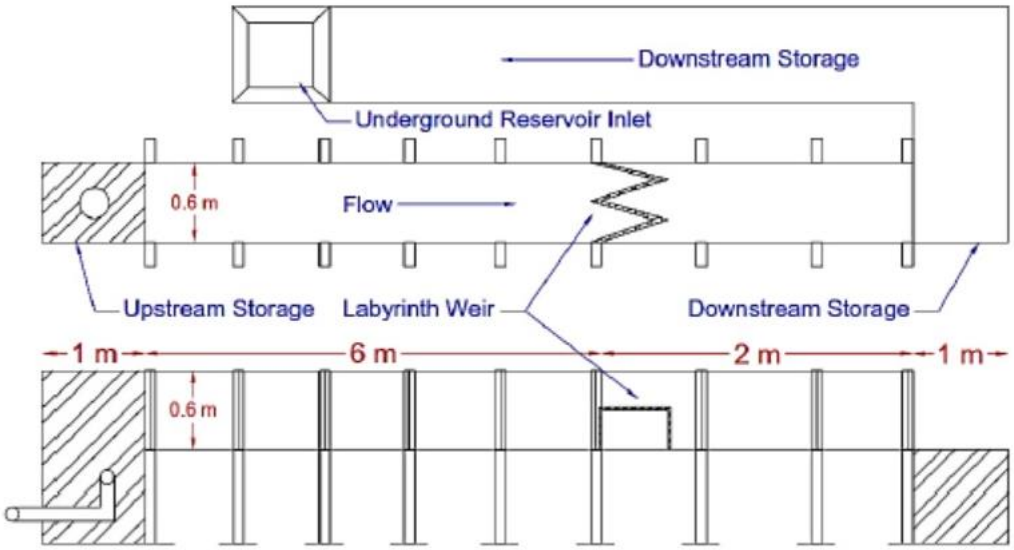


Figure 1. Layout and longitudinal section of the hydraulic flume used in this study

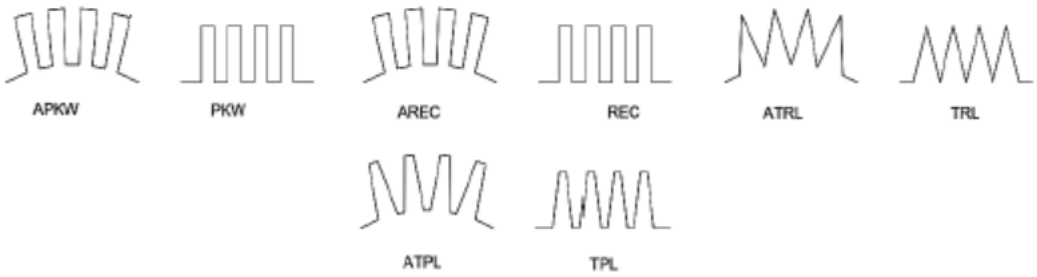


Figure 2. Plan view of the zigzag (labyrinth) and piano key weir models used in the experiments.

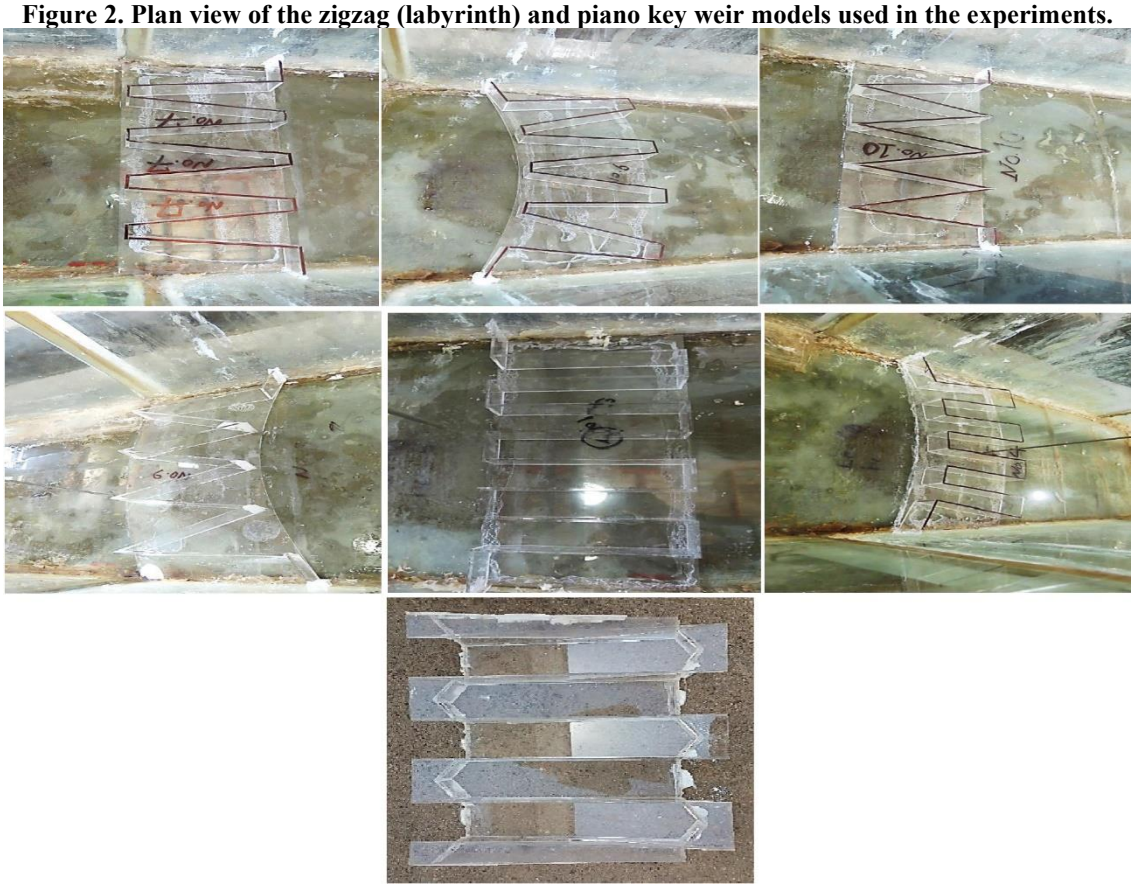


Figure 3. Physical view of the zigzag and piano key weir models used in the experimental study

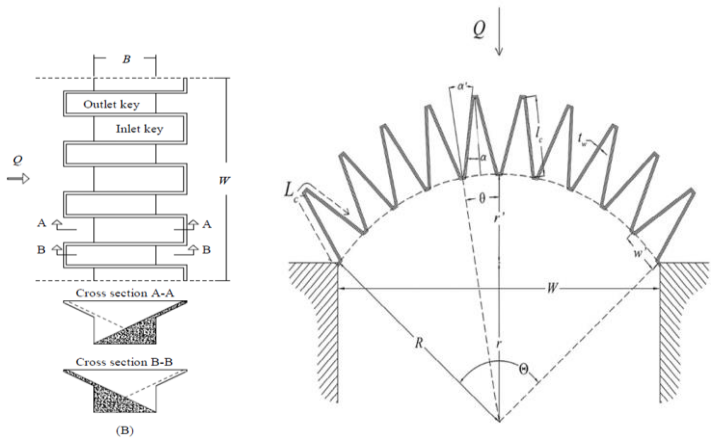


Figure 4. Schematic view of geometric dimensions of piano-key and labyrinth weirs

Table 1. Geometric dimensions and hydraulic specifications of the experimental non-linear weir models

N	L (cm)	ts (mm)	R (cm)	P (cm)	A (cm)	w (cm)	W (cm)	B (cm)	Sf
4	229.5	3	-	6	3	12	60	24.19	Trapezoidal Labyrinth (TPL)
4	236	3	63	6	3	12	60	24.12	Arc Trapezoidal Labyrinth (ATPL)
4	210	3	-	6	-	12	60	24.74	Triangular Labyrinth (TRL)
4	215	3	63	6	-	12	60	25.65	Arc Triangular Labyrinth (ATRL)
4	252	3	-	6	6	12	60	24	Rectangular Labyrinth (RCL)
4	261.19	3	63	6	6	12	60	24.08	Arced rectangular Labyrinth (ARCL)
4	252	3	-	6	6	12	60	24	Piano-key weir (PKW)
4	261.19	3	63	6	6	12	60	24.08	Arced PKW

Dimensional analysis

The discharge capacity Q of labyrinth and piano-key weirs is governed by the combined effects of approach-flow conditions, fluid properties, and the weir/channel geometry. Accordingly, the most general functional relationship may be expressed as:

$$Q=f(U, B, S, W,w, H_t, P, S_f, t_s, N, g, \mu, \rho, \sigma, y_m, P_i, P_o, B_i, B_o, B_b, W_i, W_o, L_t, S_i, S_o) \quad (2)$$

Where Q is the discharge capacity, U is mean flow velocity, B is the side wall length (wing length), S denotes the channel slope, w is the width of a single weir cycle, S_f is the weir shape factor, W is the total channel width, t_s is the weir wall thickness, P is the weir height, N is the number of cycles, H_t is the total hydraulic head, g is the gravitational acceleration, μ is the dynamic viscosity, ρ is the fluid density, σ is the surface tension, y_m is the upstream flow depth, P_i and P_o are the inlet and outlet key heights, B_b is the base length, B_i and B_o represent the upstream and downstream lengths, W_i and W_o are the inlet and outlet key widths, L_t is the total crest length, and S_i and S_o are the inlet and outlet slopes, respectively.

To derive a nondimensional formulation, the repeating variables were selected as ρ, U, and P, which collectively represent the fundamental dimensions of mass, length, and time. Applying Buckingham's π-theorem yields a general dimensionless relationship of the form:

$$Q=f(U, B, S, W,w, H_t, P, S_f, t_s, N, g, y_m, \rho, P_i, P_o, B_i, B_o, B_b, W_i, W_o, L_t, S_i, S_o) \quad (3)$$

In the present experiments, the approach flow is fully turbulent and the fluid is water under laboratory conditions. Therefore, the influence of viscous and surface-tension forces is negligible compared to inertia and gravity. This is consistent with the conventional treatment of sharp- and broad-crested weir hydraulics under high Reynolds numbers. Consequently, the Reynolds and Weber numbers do not act as active predictors in the present dataset and can be omitted, leading to:

$$f\left(\frac{Q}{L_c\sqrt{g}H_0^{1.5}}, \frac{y_m}{P}, \frac{H_t}{P}, \frac{gP}{U^2}, \frac{t_s}{P}, \frac{P_i}{P}, \frac{P_o}{P}, \frac{W}{P}, \frac{W_i}{P}, \right. \quad (4)$$

At this stage, two complementary considerations were employed to arrive at a parsimonious yet physically meaningful predictor set: (i) Dataset-driven justification (constant parameters): Several geometric variables (e.g., W, P, t_s, and other structural

dimensions) were kept constant across all tested models. Since these variables exhibit no variation within the experimental dataset, they cannot explain the observed variation of C_d and thus cannot be identified as effective predictors in a data-driven regression framework. They were therefore excluded from the final predictive formulation; (ii) Hydraulic/engineering justification (interdependent geometry). For labyrinth and piano-key weirs, many detailed geometric descriptors (e.g., Wi, Wo , Bi, Bo, Bb, Pi, Po, Si, So) are not independent in practice and often vary in a coupled manner as part of a single planform design. Including all of them separately would (a) inflate input dimensionality, (b) introduce strong collinearity among predictors, and (c) reduce the interpretability and robustness of the resulting equations- especially for transparent "white-box" models such as MARS and GEP. Accordingly, in line with established nonlinear-weir hydraulics, the geometric influence was represented using physically meaningful composite descriptors that directly reflect the dominant mechanisms controlling discharge performance. The following equation is derived based on the above-mentioned explanation:

$$f\left(\frac{Q}{L_c\sqrt{g}H_0^{1.5}}.\frac{H_t}{P}.\frac{gP}{U^2}.S,F,\right) \quad (5)$$

Accordingly, the discharge coefficient can be written as:

$$C_d=f\left(\frac{H_t}{P}.Fr.S,F,\right) \quad (6)$$

To incorporate the qualitative influence of the weir shape (S.F.) into the data-driven models, the geometric configurations were quantified using physically-based descriptors rather than arbitrary numerical labeling. Specifically, the shape effect was represented by two key dimensionless ratios: the magnification ratio $(\frac{L}{W})$, which reflects the effective crest length development, and the curvature ratio $(\frac{R}{W})$, which distinguishes between linear and arced planforms. For linear weirs, the curvature ratio was assigned a value of zero, while for arced models, the actual radius-to-width ratio was utilized. This approach ensures that the model captures the underlying hydraulic mechanisms associated with each geometry, providing a more robust physical interpretation compared to categorical indexing. Thus, the following equation was developed:

$$C_d=f\left(\frac{H_t}{P}, Fr, \frac{L}{W}, \frac{R}{W}\right) \quad (7)$$

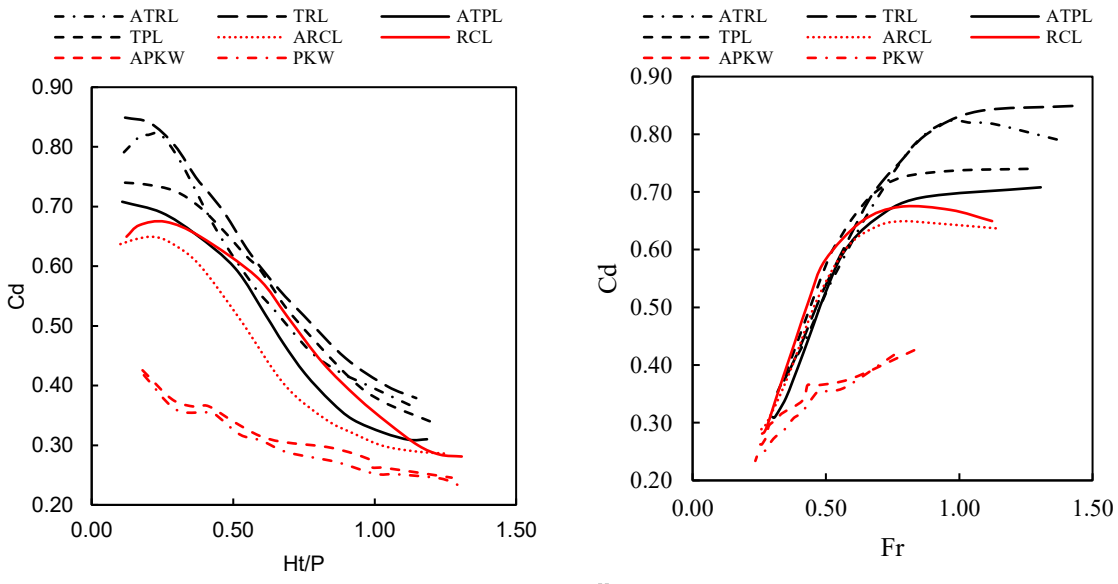


Figure 5. Experimental results of C_d-$\frac{H_t}{P}$ and C_d-Fr for weirs included

Overview on MMLs

The SVM

The SVMs demonstrate superior performance and higher generalization capabilities compared to other machine learning techniques, such as neural networks, particularly when dealing with small datasets. Furthermore, SVMs are less susceptible to overfitting, which enables them to yield more reliable and robust results. Introduced by Cortes and Vapnik [17] as a form of supervised learning, this method utilizes structural risk minimization as its objective function. By effectively mitigating overfitting, SVMs exhibit enhanced predictive performance on testing datasets. The SVMs are originally designed to classify data from different categories by constructing an optimal separating hyperplane that maximizes the margin between classes. As noted by Roushangar et al. [18], SVMs are based on the idea of structural risk minimization and are particularly effective when dealing with data that exhibit strong variability in high-dimensional spaces. The essence of this method is to transform the original feature space into a higher-dimensional space in which the classes become more separable. In this transformed space, the input data are represented as

$$X = \{(x_1.y_1).(x_2.y_2).,,,.(x_n.y_n)\} \quad (1)$$

where (x_i, y_i) denotes the i^{th} training sample. The SVM model can be written as:

$$f(x) = w^T \emptyset(x) + b \quad (2)$$

where w is the weight vector, b is the bias term, and $\emptyset(x)$ is the mapping function that projects the data into a feature space. The corresponding optimization problem is formulated as:

$$min(w.\xi.b) = \frac{1}{2}\|w\|^2 + C\sum_{i=1}^{n}\xi_i \quad (3)$$

subject to

$$\begin{cases} 1 - \xi_i - y_i(w^T\emptyset(x_i) + b) \le 0 \\ -\xi_i \le 0 \end{cases} \quad (4)$$

where C is the penalty parameter controlling the trade-off between maximizing the margin and minimizing classification error. The final regression equation is as following:

$$f(x) = \sum_{i=1}^{n} a_i K(x_i.x_j) - b \quad (5)$$

In the aforementioned formulation, K(x_i, x_j) represents the kernel transformation function. While various types of kernel functions exist, this study utilizes the Radial Basis Function (RBF)- also known as the Gaussian kernel which is one of the most widely used and powerful options. The RBF kernel is mathematically defined as:

$$K(x_i.x_j) = \varphi^T(x_i)\varphi(x_j) = exp[\frac{\|x_i - x_j\|^2}{2\sigma^2}] \quad (6)$$

where σ is a positive hyperparameter that regulates the kernel's behavior. The most critical challenge in implementing SVM lies in the optimal selection of three key hyperparameters: the penalty parameter C, the kernel parameter (σ), and the tube size (ε) [19, 20].

The GEP

This algorithm comprises a Genetic Algorithm based on Darwin's theory of evolution, utilizing a population of individuals selected according to their fitness. Genetic modifications are subsequently applied through one or more genetic operators. The flowchart of the GEP process is illustrated in Fig. 6 [21]. The first step involves generating an initial population of formulas, created by the random combination of a set of functions (mathematical operators) and terminals (problem variables and constants). In the second step, each individual in the population is evaluated using specific fitness criteria. The third step entails the generation of a new population of formulas, and the final step involves repeating the process until the maximum number of generations is reached [22].

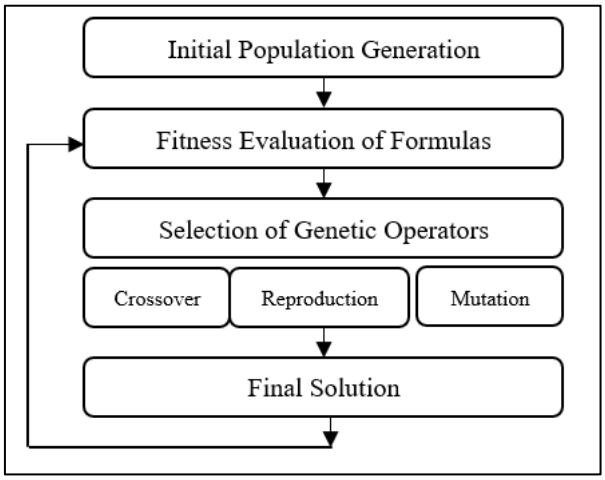


Figure 6. The flowchart of the GEP model

The MARS

The MARS technique was originally introduced by Friedman [23]. Operating as a non-parametric statistical approach, MARS partitions the input space into distinct sub-regions. Within each segment, specialized basis functions known as splines are employed to establish a precise mathematical link between the predictors and the response variable. The general analytical structure of the model developed through this procedure is detailed in Eq. 7:

$$n = C_o + \sum_{i=1}^{N} C_i \prod_{j=1}^{K_j} B_{ij}\,(y_{v(j.i)}) \quad (7)$$

In this formulation, n represents the target variable, while C_0 denotes the model's constant intercept, the term C_i refers to the weighting coefficients assigned to each basis function, v(j,i) identifies the specific input feature for the j^{th} component of the i^{th} term. Additionally, k_j defines the constraint on the degree of interaction between variables. The analytical representation of the fitted splines is formulated as follows:

$$B_{ji}(y)=(y-t_{ji})_{+}^{q}=\begin{cases}(y-t_{ji})^{q} & y<t_{ji}\\ 0 & \text{otherwise}\end{cases} \quad (8)$$

$$B_{ji+1}(y)=(t_{ji}-y)_{+}^{q}=\begin{cases}(y-t_{ji})^{q} & y<t_{ji}\\ 0 & \text{otherwise}\end{cases}$$

Here, t_{ji} denotes the spline knots. The construction of a MARS-based model involves a dual-phase procedure. The initial phase, known as the 'forward pass' or growth stage, entails partitioning the input feature space into numerous computational sub-regions and generating an extensive set of basis functions (splines). Subsequently, to enhance the model's generalization capability and mitigate the risk of overfitting (local performance bias), a backward pass or pruning stage is executed. During this phase, redundant splines are systematically eliminated to optimize the model's complexity. The selection for pruning is governed by the minimization of the Residual Sum of Squares (RSS) within the training dataset, which is defined as follows:

$$RSS = \sum_{i=1}^{N}(n_i - f_i)^2 \quad (9)$$

In this context, n_i represents the experimentally observed values, while f_i denotes the corresponding values estimated by the model. To evaluate the robustness and predictive performance of the basis functions, the Generalized Cross-Validation (GCV) criterion is employed. The GCV index is determined using the following expression:

$$GCV = \frac{RSS}{N[1-\frac{C(B)}{N}]^2} \quad (10)$$

Within the GCV framework, N signifies the total sample size of the dataset, while C(B) represents the complexity penalty factor. This penalty term, which accounts for the number of basis functions to prevent model over-complexity, is derived as follows:

$$C(B) = B + d[\frac{B-1}{2}] \quad (11)$$

In this expression, B denotes the total count of basis functions utilized in the model, while d represents the cost (penalty) associated with each individual basis function incorporated during the process [24].

Model Evaluation Criteria

To evaluate the predictive precision and the robustness of the developed models, four distinct statistical performance measures were employed. These include the Root Mean Square Error (RMSE), Mean Absolute Error (MAE), Coefficient of Determination (R^2), and the Developed Discrepancy Ratio (DDR). The mathematical formulations for these metrics, as adopted from the study by Kisi et al. [25], are presented below:

$$RMSE=\sqrt{\frac{1}{n}\sum_{i=1}^{n}(y_i\hat{y}_i)^2} \quad (12)$$

$$MAE=\frac{\sum_{i=1}^{n}|y_i\hat{y}_i|}{n} \quad (13)$$

$$R^2=1\frac{\sum_{i=1}^{n}(y_i\hat{y}_i)^2}{\sum_{i=1}^{n}(y_i\bar{y})^2} \quad (14)$$

$$DDR=\frac{\text{Predicted value}}{\text{Observed value}}-1 \quad (15)$$

In these expressions, n represents the total number of observations, y_i denotes the measured (actual) value, and $\hat{y}_i$ corresponds to the model-predicted value for the i^{th} observation. Collectively, these performance indicators provide a comprehensive assessment of model behavior by quantifying prediction accuracy, error magnitude, the proportion of explained variance, and potential prediction bias. Among them, the DDR is particularly effective in detecting systematic tendencies toward overestimation or underestimation. For more advanced analyses, normalized variants such as X_{DDR} and Z_{DDR} have been introduced to enhance bias identification and facilitate clearer visual interpretation of model performance [26].

Results

The outcomes of SVM

The SVM model was implemented in the MATLAB environment using a total of 96 experimental data points to predict Cd. To ensure a robust evaluation of the model's generalization capability, the dataset was partitioned into 80% for the training phase (76 samples) and 20% for the testing phase (20 samples). To identify the optimal model architecture, an extensive trial-and-error process was conducted, involving a wide range of combinations for the tuning parameters (C, γ, ε). While numerous configurations were tested, five representative groups- including the best-performing combination and four others with varying degrees of accuracy- are summarized in Table 2 for comparison. The results indicate that Group 1 is the superior configuration, yielding the highest $C_{d(DDR(max))}$ values (2.515 in training and 2.277 in testing). The stability of the error metrics (e.g., RMSE of 0.067 and 0.075) across both phases confirms that this specific combination effectively captured the non-linear relationship between the four independent variables and Cd. In contrast, the other four groups (Groups 2–5) demonstrate the sensitivity of the SVM model to hyperparameter selection. For instance, the drastic decline in $C_{d(DDR(max))}$ in Group 4 (dropping to 0.080) coupled with a substantial increase in RMSE, illustrates how sub-optimal parameters can lead to significant predictive bias. These comparisons underscore that among the wide array of tested parameters, the configuration in Group 1 provides the most reliable and high-fidelity framework for this hydraulic modeling task.

Table 2. Performance metrics of SVM models with different tuning parameters.

	Tuning parameters			Training phase				Testing phase			
	C	γ	ε	RMSE	MAE	R^2	$C_{d(DDR(max))}$	RMSE	MAE	R^2	$C_{d(DDR(max))}$
Group 1	1.0	0.01	0.2	0.067	0.056	0.864	2.515	0.075	0.066	0.843	2.277
Group 2	1.5	0.05	0.01	0.393	0.314	0.442	0.631	0.324	0.260	0.673	0.839
Group 3	3	0.2	0.05	0.234	0.189	0.364	0.895	0.279	0.227	0.521	0.790
Group 4	10	0.5	0.5	5.180	4.004	0.447	0.080	0.508	0.397	0.579	0.545
Group 5	25	1	0.1	0.473	0.374	0.349	0.504	0.340	0.285	0.344	0.625

The graphical comparison between the experimental measurements and SVM predictions (Fig. 7) demonstrates a high degree of synchronization in both phases. The model effectively tracks the periodic fluctuations of the discharge coefficient, successfully capturing the peak and valley trends across the entire range of test conditions. While the training phase shows a near-perfect overlap, the testing phase reveals minor localized discrepancies, particularly at extreme peak points. These slight deviations occur where hydraulic gradients are most abrupt; however, the model maintains the correct phase and trend without significant lag. The consistent alignment between the two lines confirms the model's robustness and high predictive accuracy for unseen data.

The $C_{d(DDR)}$ plots (Fig. 8) illustrate the error distribution characteristics for the five investigated groups. A more reliable and robust model is identified by a higher peak value of the Gaussian function $C_{d(DDR)max}$ and a narrower distribution centered around zero. As shown in Fig. 8, Group 1 (represented by blue squares) exhibits the highest peak in both training and testing phases, significantly outperforming the other configurations. This indicates that a larger portion of the predicted values for Group 1 falls within a very narrow range of the actual experimental data, signifying superior precision. In contrast, Group 4 and Group 5 show flatter curves with lower peak values, reflecting higher dispersion and lower predictive reliability. The consistency of Group 1's dominant peak across both phases confirms its high generalization capability and minimal systematic bias.

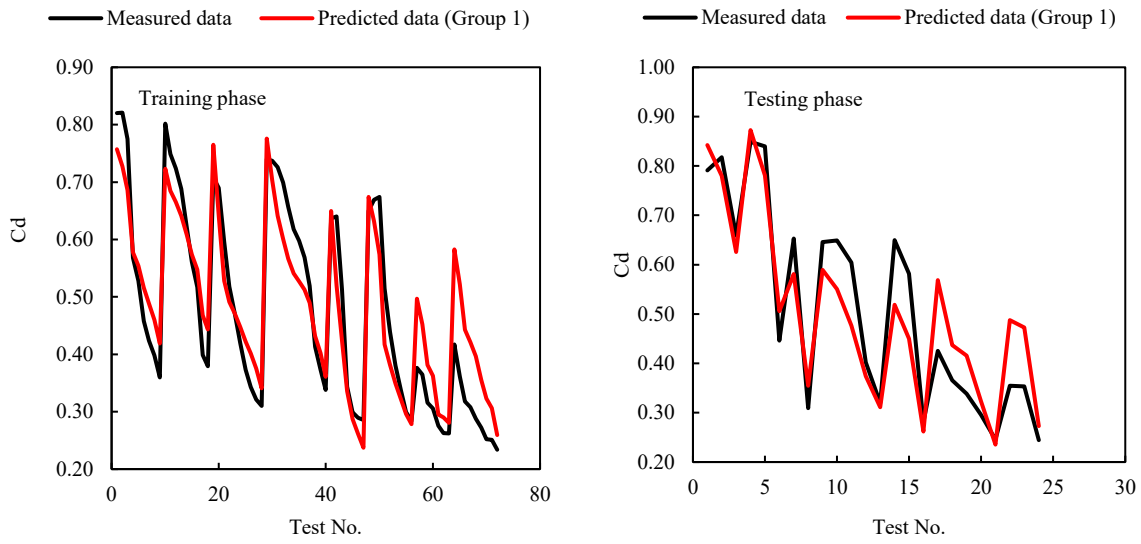


Figure 7. Comparison of measured vs. predicted C_d for the SVM model

The $C_{d(DDR)}$ plots (Fig. 8) illustrate the error distribution characteristics for the five investigated groups. A more reliable and robust model is identified by a higher peak value of the Gaussian function $C_{d(DDR)max}$ and a narrower distribution centered around zero. As shown in Fig. 8, Group 1 (represented by blue squares) exhibits the highest peak in both training and testing phases, significantly outperforming the other configurations. This indicates that a larger portion of the predicted values for Group 1 falls within a very narrow range of the actual experimental data, signifying superior precision. In contrast, Group 4 and Group 5 show flatter curves with lower peak values, reflecting higher dispersion and lower predictive reliability. The consistency of Group 1's dominant peak across both phases confirms its high generalization capability and minimal systematic bias.

The scatter plots (Fig. 9) provide a visual assessment of the model's predictive performance relative to the ideal 1:1 agreement line. A high concentration of data points around the diagonal line signifies a robust correlation and low residual errors. In the training phase, the data points are densely clustered along the 45-degree line, indicating that the SVM model has successfully learned the underlying non-linear relationships. In the testing phase, the points remain closely distributed around the identity line, confirming the model's generalization capability. Although a few points show slight scattering—particularly in the mid-range of C_d values ($0.4 < C_d < 0.6$)- the lack of significant systematic bias (overestimation or underestimation) across the entire range proves that the model is highly reliable for hydraulic coefficient estimation.

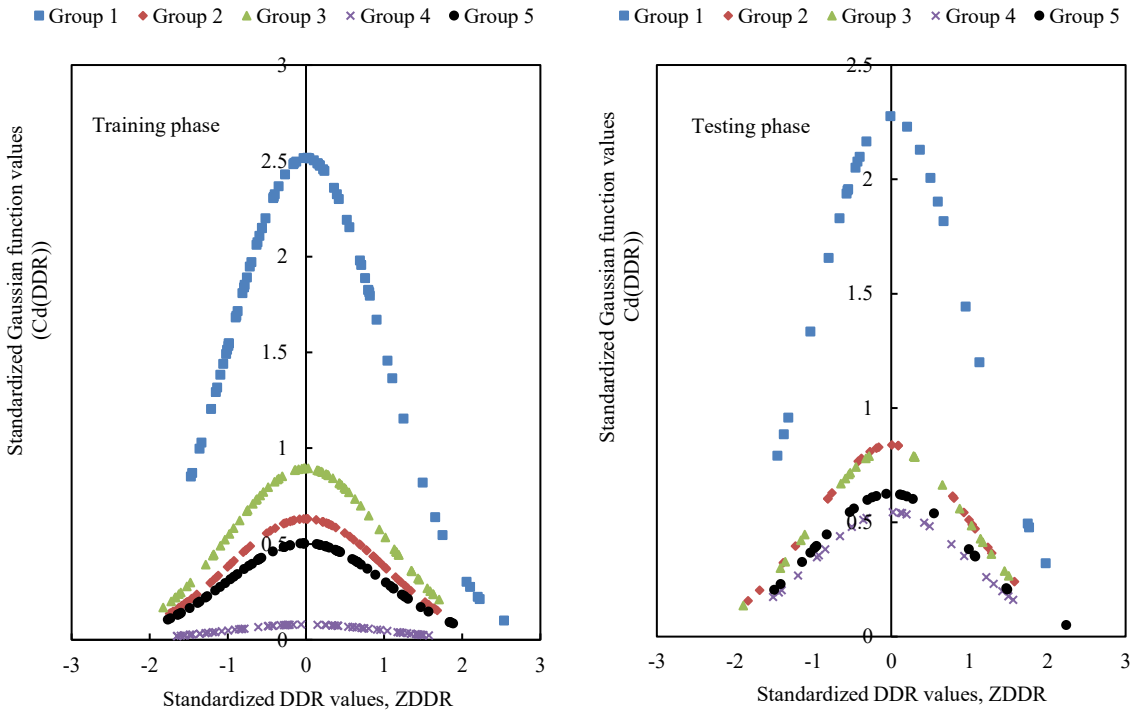


Figure 8. The DDR distribution for various SVM groups in training and testing phases

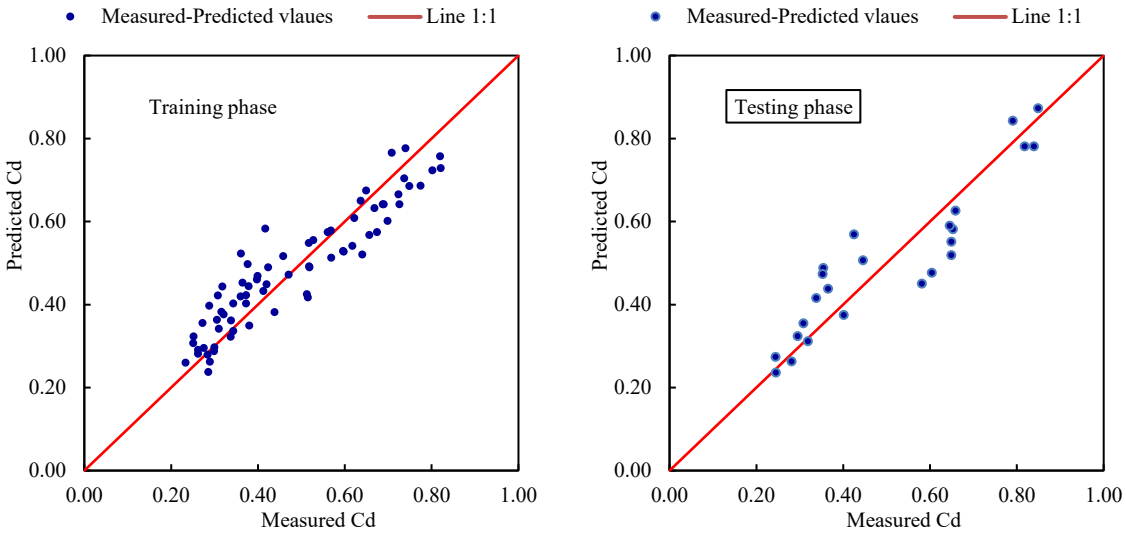


Figure 9. Scatter plots of measured vs. predicted Cd values for the SVM model

The density-based scatter plots (Fig. 10) provide a deeper insight into the concentration of data points and the local accuracy of the model. The color gradient, ranging from red (low density) to dark blue (high density), illustrates where the majority of predictions are clustered. In both the training and testing phases, the high-density kernels (blue regions) are strictly aligned along the diagonal axis. This alignment indicates that for the most frequent experimental conditions, the SVM model's predictions are highly concentrated around the measured values, reflecting minimal local variance. The formation of distinct density islands suggests that the model maintains its precision across different regimes of the C_d, from low to high values. The sharp transition from blue to red around the diagonal further confirms that large outliers are rare, reinforcing the statistical reliability and robustness of the developed model.

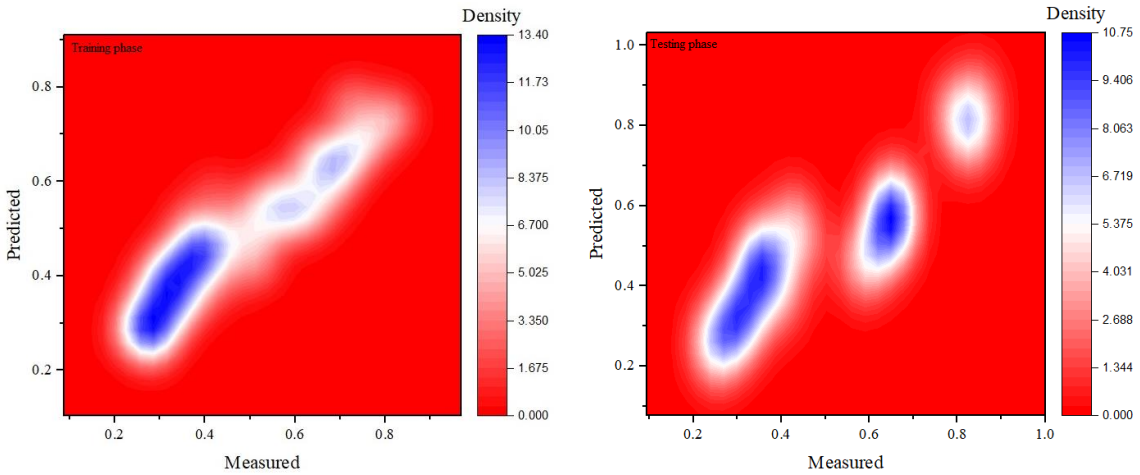


Figure 10. Kernel density plots of measured versus predicted C_d for the SVM model

The outcomes of GEP

The GEP model was implemented and executed within the GeneXproTools environment, utilizing a total of 96 experimental data points. The dataset was randomly partitioned into two subsets: 80% (76 points) for the training phase to evolve the symbolic expressions, and the remaining 20% (20 points) for the testing phase to verify the model's generalization capacity. The performance metrics, as summarized in Table 3, highlight the significant impact of architectural settings on the prediction of C_d. Evaluation of the five investigated groups reveals that Group 1- configured with 30 chromosomes and a head size of 8- yields the most robust results. This configuration achieved the lowest error margins (RMSE=0.032) and an excellent correlation (R^2=0.967) during training, which remained consistently high in the testing stage (R^2=0.959). The high $C_{d(DDR)max}$ value of 5.648 for this group further confirms its superior precision in centering residuals around zero. These findings indicate that the evolutionary process in Group 1 successfully captured the underlying hydraulic patterns without overfitting, despite the limited size of the testing dataset. Fig. 11 illustrates the Expression Tree (ET) of an optimized GEP model, consisting of three Sub-ETs. It represents a complex mathematical formula where functional nodes (operators like *, +, Exp, Sqrt) process terminal nodes to generate a predictive symbolic output. The mathematical form of the ET's outcome is presented in Eq. 16.

Table 3. Evaluation of GEP model efficiency across different structural configurations

	Tuning parameters				Training phase				Training phase			
	Chromosome number	Head size	Gene number	Combination	RMSE	MAE	R^2	$C_{d(DDR(max)}$	RMSE	MAE	R^2	$C_{d(DDR(max)}$
Group 1	30	8	3	+	0.032	0.024	0.967	5.648	0.041	0.029	0.959	5.418
Group 2	40	8	3	+	0.419	0.336	0.237	0.548	0.205	0.169	0.574	1.071
Group 3	20	15	4		0.165	0.132	0.487	1.376	0.091	0.071	0.836	2.184
Group 4	30	20	5	/	0.146	0.124	0.557	1.468	0.104	0.076	0.763	2.155
Group 5	30	25	7	+	0.166	0.135	0.552	1.298	0.123	0.103	0.763	1.946

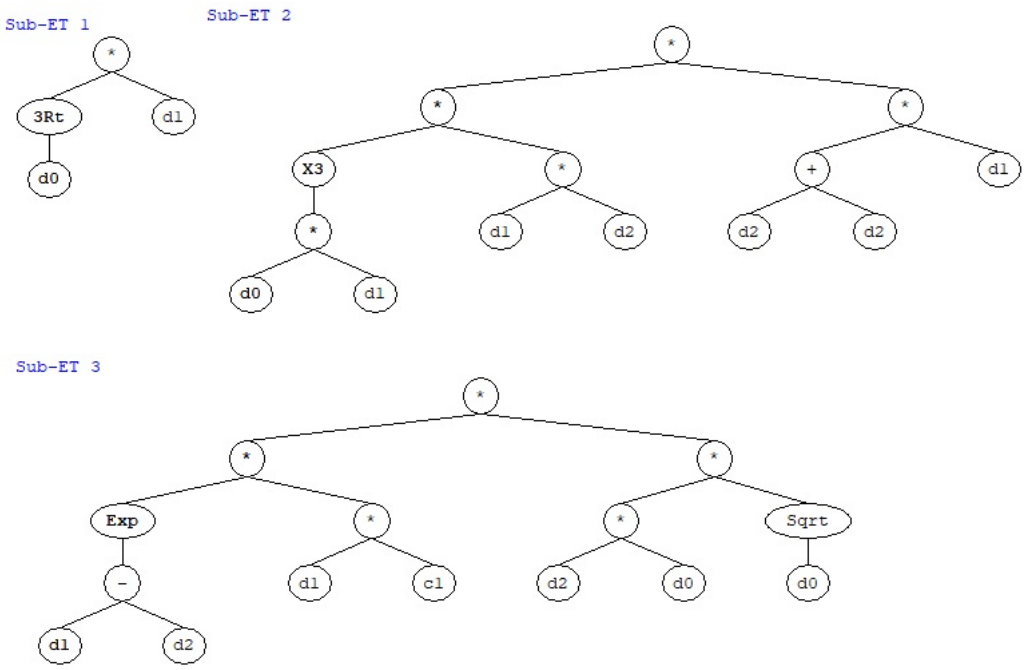


Figure 11. Expression tree of optimized model of GEP

$$C_d=\sqrt[3]{\frac{H_t}{P}}\times Fr+[(\frac{H_t}{P}\times Fr)^3\times(Fr\times\frac{L}{W})]\times[(2\frac{L}{W})\times Fr]+[(Exp(Fr-\frac{L}{W})\times(-2{,}83Fr)]\times[(\frac{H_t}{P}\times\frac{L}{W})\times\sqrt{\frac{H_t}{P}}] \quad (16)$$

The response of the optimal GEP model (Group 1) in estimating the C_d is visualized in Fig. 12. A primary observation is the exceptional synchronization between the symbolic model's output and the experimental observations. The GEP-derived formulation shows an inherent ability to mimic the high-frequency fluctuations of the hydraulic data, particularly in the training phase where the two lines are virtually indistinguishable. In the validation (testing) phase, the model maintains a robust trend-following behavior. Unlike black-box models that may struggle with extreme data points, the GEP model accurately captures the magnitude of the peaks. The absence of any significant offset or lag between the predicted and measured values confirms that the evolutionary algorithm has successfully simplified the complex non-linear physics of the flow into a reliable predictive tool. This level of point-to-point correspondence validates the high generalization potential of the developed equation for practical engineering applications.

The error distribution profiles for the GEP groups are presented in Fig. 13 using a standardized Gaussian framework. The diagnostic value of these plots lies in the height and steepness of the curves; a pronounced peak indicates that the model's predictions are highly centered on the actual values with minimal deviation. A comparative look at the results reveals that Group 1 (blue markers) stands out with a remarkably high $C_{d(DDR)max}$ value exceeding 5.0 in both phases. This sharp, bell-shaped distribution signifies a low-variance prediction regime, where the majority of the computed C_d values align precisely with the zero-error axis. In contrast, the remaining groups (Groups 2 through 5) display significantly flatter and broader distributions, indicating a higher frequency of larger residuals and lower reliability. The stability of the high-peak profile for Group 1 from training to testing demonstrates that the genetic evolution successfully converged on a stable mathematical solution with high statistical confidence.

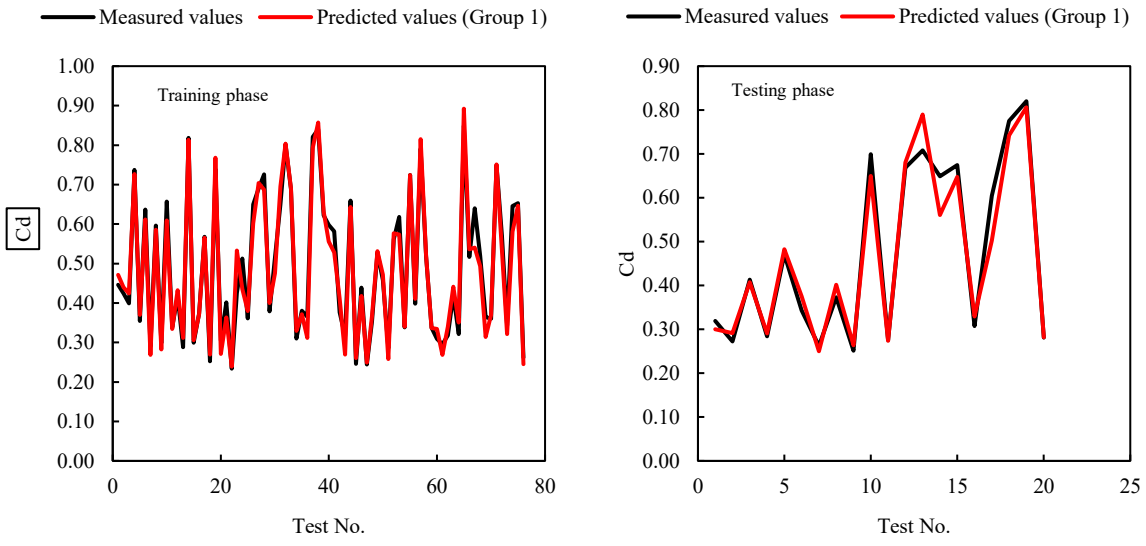


Figure 12. Comparison of measured vs. predicted C_d for the GEP model

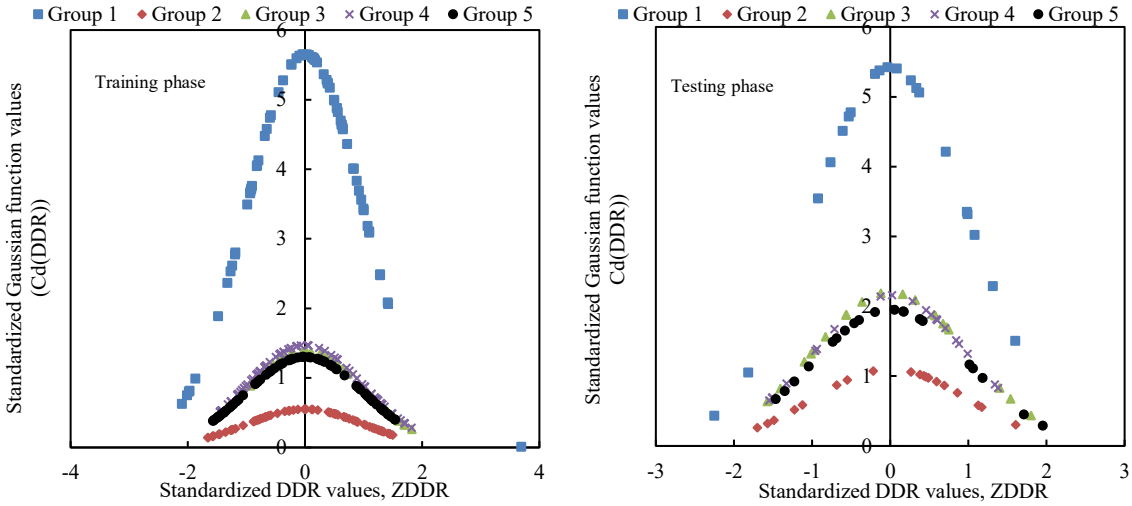


Figure 13. The DDR distribution for various GEP groups in training and testing phases

The concentration of GEP predictions relative to experimental benchmarks is explored through the kernel density plots in Fig. 14. In the training stage, the formation of a continuous high-density ridge along the diagonal suggests that the GEP algorithm has successfully captured the global trend of the discharge coefficient. More importantly, the testing phase exhibits a sharp, localized density peak (with a value reaching approximately 39.0) in the lower C_d range. This indicates an exceptional level of precision for specific hydraulic conditions, where the variance between predicted and actual values is nearly negligible. The narrow width of the white and blue envelopes across the entire range confirms that the GEP model maintains consistent predictive integrity without suffering from significant data dispersion or heteroscedasticity.

The correlation between the observed hydraulic measurements and the GEP-formulated predictions is visualized through the scatter diagrams in Fig. 15. In the training phase, the points show remarkably low dispersion, reflecting the high-fidelity mapping successfully performed by the evolutionary symbolic search. More importantly, this tight adherence to the diagonal reference is preserved in the testing phase. Unseen data points show virtually no significant scatter or outward deviation, even in the higher ranges where hydraulic instabilities typically degrade model accuracy. This uniform distribution across the entire spectrum of C_d values confirms that the GEP model provides an unbiased, mathematically stable, and highly generalizable representation of the C_d.

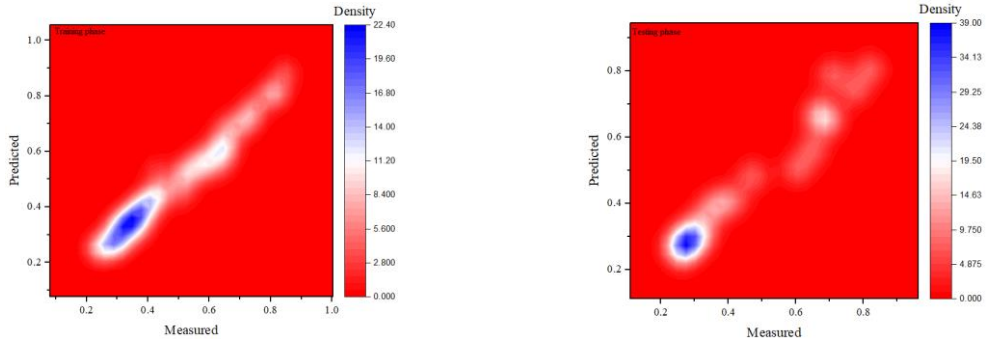


Figure 14. Kernel density plots of measured versus predicted C_d for the GEP model

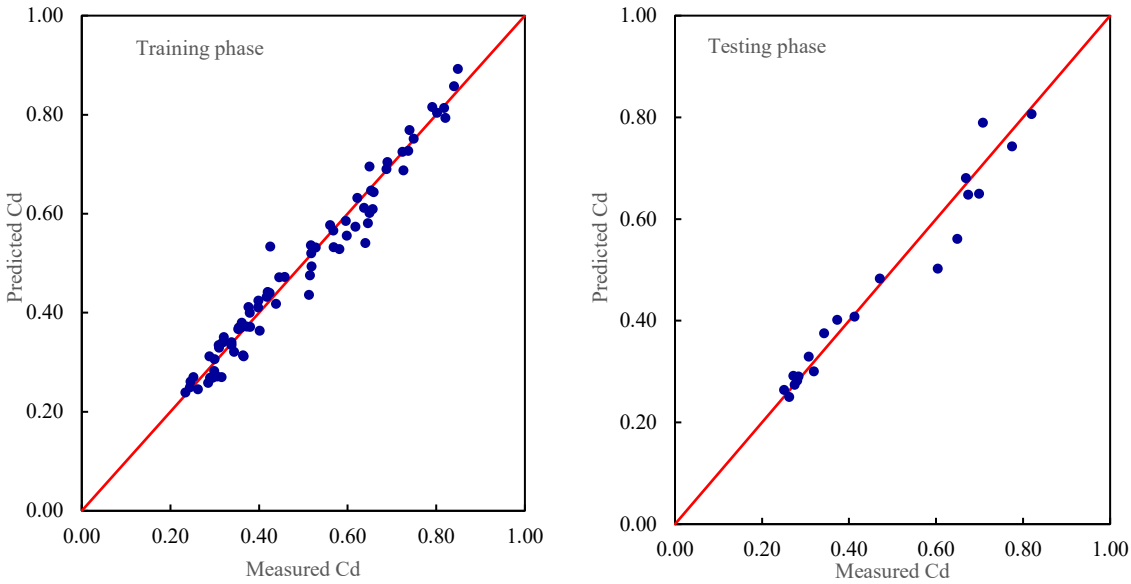


Figure 15. Scatter plots of measured vs. predicted C_d values for the GEP model

The outcomes of MARS

The MARS model was developed and implemented within the MATLAB environment. Through a systematic trial-and-error process, the influence of various tuning parameters was evaluated using a total of 96 experimental samples (76 for training and 20 for testing), as summarized in Table 4. The results show that predictive accuracy significantly improves as the model transitions from Group 1 to Group 3. Interestingly, Groups 3, 4, and 5 exhibit nearly identical performance metrics, all achieving the highest observed $C_{d(DDR)max}$ (approx. 8.81 in training and 6.63 in testing) alongside an R^2 of 0.9882. However, these groups differ in their structural complexity: Group 3 utilizes 31 basis functions with a second-order interaction, while Group 5 expands to 41 functions and a third-order interaction. Despite the similarity in statistical indices, Group 5 is highlighted as the most comprehensive configuration, as it demonstrates that increasing the interaction degree to 3 and max basis functions to 41 maintains peak stability and performance without leading to overfitting. This suggests that the model has reached its maximum potential for accuracy and reliability within these parameter ranges, with the $C_{d(DDR)max}$ index confirming the superior robustness of these advanced configurations over the simpler ones.

Table 4. Optimization settings of MARS model to predict C_d

	Tuning parameters					Training phase				Training phase			
	Max Basis Functions	Interaction Degree	Penalty	Threshold	Pruning	RMSE	MAE	R^2	$C_{d(DDR(max)}$	RMSE	MAE	R^2	$C_{d(DDR(max)}$
Group 1	21	1	2	0.0005	Yes	0.0349	0.0269	0.9618	5.6191	0.0510	0.0353	0.9281	3.5689
Group 2	21	2	2	0.0005	Yes	0.0212	0.0174	0.9860	7.7602	0.0496	0.0333	0.9286	3.3730
Group 3	31	2	2	0.0005	Yes	0.0194	0.0157	0.9882	8.8139	0.0266	0.0170	0.9792	6.6325
Group 4	31	2	3	0.0005	Yes	0.0194	0.0157	0.9882	8.8139	0.0266	0.0170	0.9792	6.6331
Group 5	41	3	2	0.0005	Yes	0.0194	0.0157	0.9882	8.8139	0.0266	0.0170	0.9792	6.6331

Table 5. Model summary of optimum MARS model

	Value
Independents	4
Dependents	1
Number of terms	12
Number of basis functions	16
Order of interactions	3
Penalty	2.0
Threshold	0.0005
GCV error	0.000777
Prune	Yes

Table 5 presents the structural characteristics and final hyperparameter configuration of the optimized MARS model. The model utilizes 4 independent variables to predict a single dependent output through a pruned architecture. A critical aspect of this configuration is the selection of 12 terms derived from 16 basis functions, indicating that the pruning process effectively eliminated redundant functions to enhance model parsimony. The inclusion of third-order interactions allows the model to capture complex, non-linear dependencies between the input features. Furthermore, the exceptionally low GCV (Generalized Cross-Validation) error of 0.000777 serves as a robust indicator of the model's superior generalization capability, confirming that the trade-off between model complexity and predictive accuracy has been optimally balanced.

Table 6 details the mathematical structure of the optimum MARS model by listing the intercept, basis function coefficients, and corresponding knot values for each input variable. The model's transparency is highlighted through the explicit definition of 11 terms plus an intercept. The listed knot values (shown in red) represent the critical thresholds where the slope of the regression function changes, allowing the model to adapt to local non-linearities in the data. Notably, the model incorporates both univariate terms (e.g., Term 1 and 11) and interaction terms (e.g., Terms 5, 9, and 10), which involve multiple predictors such as $\frac{H_t}{P}$ and Fr. These interactions demonstrate the model's ability to capture the synergistic effects between different hydraulic or geometric parameters. The varying magnitudes and signs of the C_d reflect the relative weight and direction of impact each basis function has on the final output. This tabular representation serves as the basis for the model's governing equation, providing a clear "white-box" alternative to traditional "black-box" machine learning algorithms.

Table 6. Optimum MARS models' coefficients

Coefficients, knots and basis functions	C_d	$\frac{H_t}{P}$	Fr	$\frac{L}{W}$	$\frac{R}{W}$
Intercept	0.45414				
Term.1	2.28129		0.603700		
Term.2	-1.88079		0.603700		
Term.3	0.52329	0.412540			
Term.4	-2.28351	0.412540			
Term.5	-4.98839	0.412540	0.772700		
Term.6	0.25689			3.500000	
Term.7	-0.43517	0.754000		3.500000	
Term.8	0.29074		0.603700	4.200000	
Term.9	4.75879	0.412540	0.431600		
Term.10	2.55213	0.584600	0.324200		
Term.11	0.01341				0.00

Table 7. Frequency of Predictor References in MARS Basis Functions

Dependents	References (to basis functions)
$\frac{H_t}{P}$	6
Fr	6
$\frac{L}{W}$	3
$\frac{R}{W}$	1

Table 7 illustrates the relative importance of each predictor by quantifying its frequency of reference within the MARS model's basis functions. The data reveals that $\frac{H_t}{P}$ and Fr are the most influential parameters, each being referenced 6 times. This high frequency indicates that these two variables play a dominant role in defining the model's non-linear structure and are critical for capturing the primary variations in the target output. In contrast, geometric ratios such as $\frac{L}{W}$ and $\frac{R}{W}$ show lower frequencies (3 and 1, respectively), suggesting they serve as secondary or refinement factors in the model. This hierarchical distribution of references provides a clear insight into the sensitivity of the model to different inputs, confirming that hydraulic conditions (represented by $\frac{H_t}{P}$ and Fr) have a more substantial impact on the prediction performance than the purely geometric constraints in this specific study.

Eq. 17 explains the extracted equation to simulate C_d using independent variables:

$$\begin{aligned} C_d = {} & 0{,}454 + 2{,}281\max(0.Fr - 0{,}6037) - 1{,}8 \\ & +0{,}5233\max\left(0.\frac{H_t}{P} - 0{,}4125\right) - 2{,}2835\,r \\ & -4{,}988\max\left(0.0{,}4125 - \frac{H_t}{P}\right)\max(0.Fr - \\ & +0{,}2569\max\left(0.\frac{L}{W} - 3{,}5\right) \\ & +0{,}2907\max(0.Fr - 0{,}3067)\max\left(0.4{,}2\right. \\ & +4{,}75\max\left(0.\frac{H_t}{P} - 0{,}4125\right)\max(0.Fr - \\ & +0{,}01342\max\left(0.\frac{R}{W}\right), \end{aligned} \quad (17)$$

Fig. 16 demonstrates the high-fidelity tracking of experimental C_d values by the optimized MARS model across both phases. The near-perfect spatial synchronization between the predicted and measured profiles indicates the model's success in capturing non-linear oscillations and sharp gradients. The lack of significant residual divergence in the testing subset confirms strong generalization capability, proving that the model accurately reflects the underlying physical mechanism rather than just fitting the training noise.

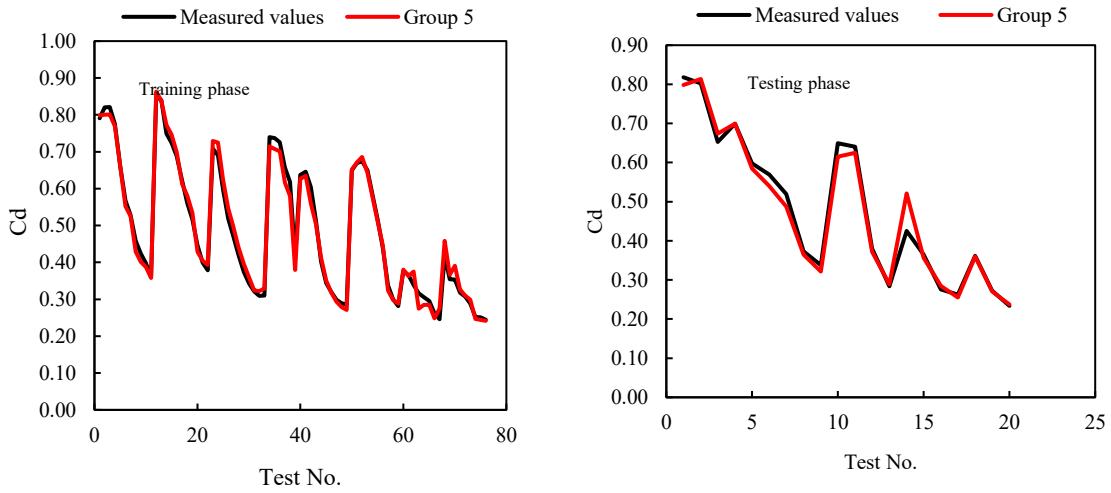


Figure 16. Comparison of measured vs. predicted C_d for the MARS model

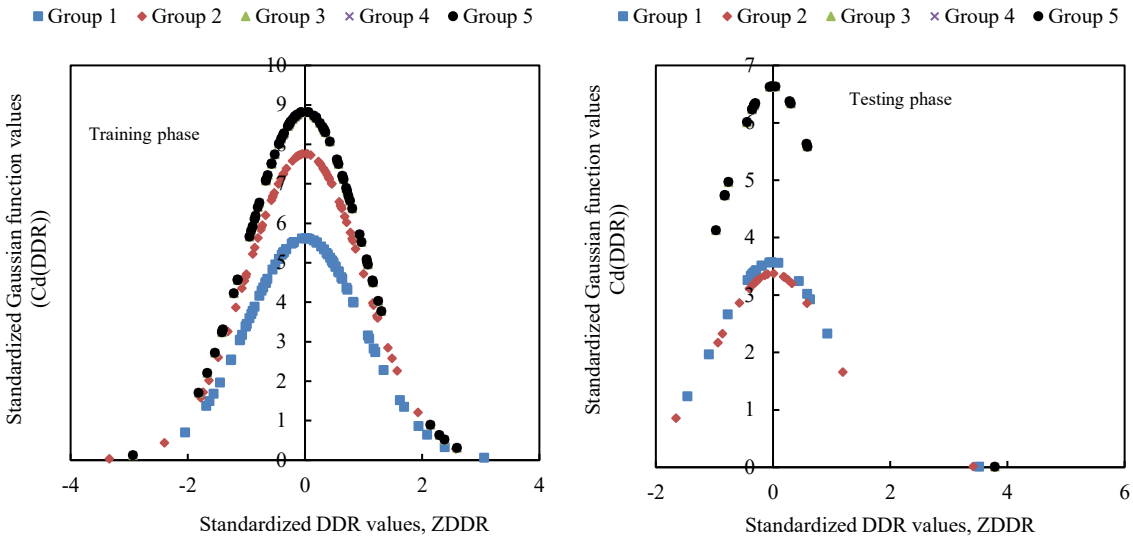


Figure 17. The DDR distribution for various MARS groups in training and testing phases

The Gaussian distribution of the DDR indices in Fig. 17 provides a probabilistic validation of model stability. The Group 5 configuration exhibits the most prominent vertical peak and the narrowest lateral spread, signifying a higher degree of statistical concentration around the optimal prediction zone. This superior peak amplitude, consistently observed in both training and testing phases, confirms that Group 5 minimizes stochastic variance and achieves the highest reliability density among the evaluated models. Consequently, the results highlight the robust generalization and enhanced predictive certainty of the optimized MARS architecture.

The KDE plots in Fig. 18 demonstrate a robust probabilistic alignment between the measured and predicted C_d values. The concentration of high-density kernels (blue regions) along the 45° bisector confirms high spatial correlation and negligible systematic bias. This tight distribution across both training and testing phases indicates minimal predictive dispersion, verifying the model's ability to maintain probabilistic certainty and excellent generalization across the experimental domain.

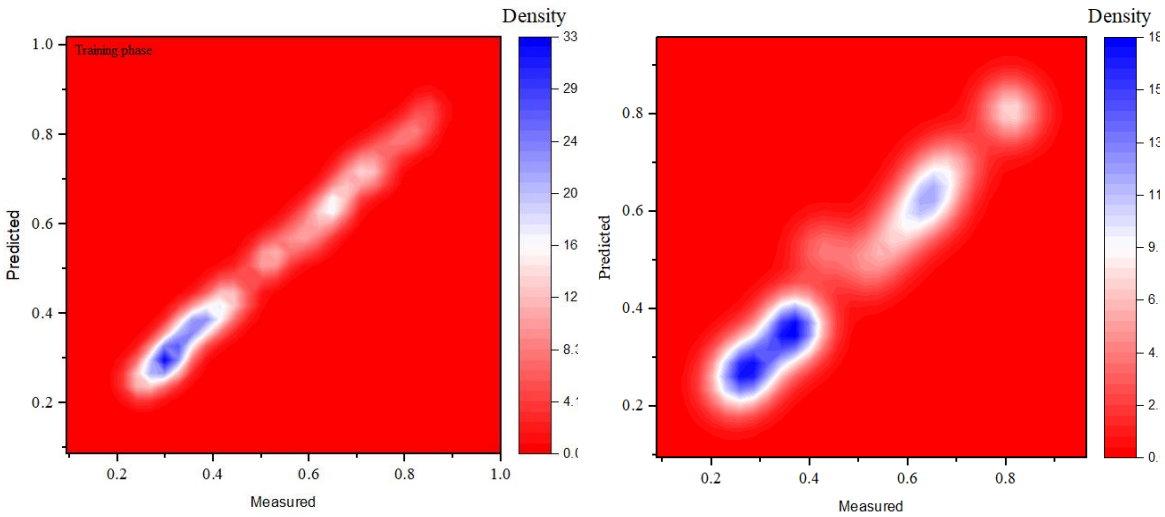


Figure 18. Kernel density plots of measured versus predicted C_d for the MARS model

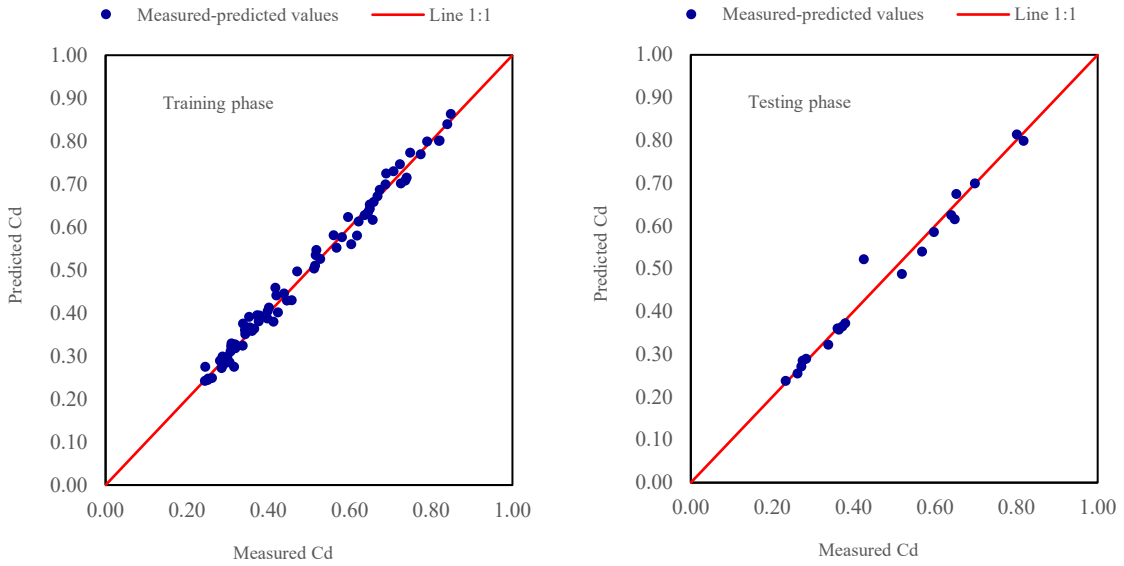


Figure 19. Scatter plots of measured vs. predicted C_d values for the MARS model

The scatter plots in Fig. 19 validate the predictive accuracy of the MARS model by demonstrating a high-fidelity alignment between measured and predicted C_d values. The dense clustering of data points around the 1:1 identity line across both training and testing phases indicates negligible systematic bias and high correlation efficiency. The absence of significant heteroscedasticity or outliers suggests that the model maintains structural stability and robust generalization capability, accurately capturing the non-linear hydraulic behavior of the discharge coefficient.

Table 8 presents a comparative performance analysis of MARS, SVM, and GEP models. The MARS model demonstrates clear statistical superiority, achieving the highest correlation (R^2=0.9882) and the lowest error metrics (RMSE=0.0194, MAE=0.0157) in the training phase. This trend persists in the testing phase, where MARS maintains a superior R^2 of 0.9792, significantly outperforming SVM and GEP. Notably, the $C_{d(DDR)max}$ index for MARS (8.8139 in training and 6.6331 in testing) is substantially higher than the competing models, confirming its exceptional predictive stability and robustness. These results identify MARS as the most reliable machine learning architecture for accurately modeling the discharge coefficient.

Table 8. An overall comparison between MLMs included to predict C_d

Model name	Training phase				Training phase			
	RMSE	MAE	R^2	$C_{d(DDR(max)}$	RMSE	MAE	R^2	$C_{d(DDR(max)}$
MARS	0.0194	0.0157	0.9882	8.8139	0.0266	0.0170	0.9792	6.6331
SVM	0.067	0.056	0.864	2.515	0.075	0.066	0.843	2.277
GEP	0.032	0.024	0.967	5.648	0.041	0.029	0.959	5.418

The Taylor diagram is a powerful graphical tool that provides a concise statistical summary of how well a model matches observations. It simultaneously displays three vital statistics: the standard deviation (which indicates the amplitude of variation), the root-mean-square error (RMSE), and the Pearson correlation coefficient. On this diagram, the Reference point on the abscissa represents the observed (target) data, where the standard deviation of the model equals that of the observations, the RMSE is zero, and the correlation coefficient is unity. Figure 20 illustrates the Taylor diagram comparison for the SVM, GEP, and MARS models during both the training and testing phases. As shown in the diagrams, the MARS model exhibits the highest performance among the developed models. It is positioned closest to the Reference point in both phases, indicating that it possesses a standard deviation nearest to the observed data, the lowest RMSE, and the highest correlation coefficient. While the GEP model also demonstrates reliable accuracy, it is slightly further from the target point compared to the MARS model. The SVM model, although providing acceptable results, shows a greater distance from the reference point in both the training and testing phases, implying a relatively higher RMSE and lower correlation compared to the other two approaches. Overall, the visual proximity of the MARS model to the reference point confirms its superior capability in capturing the discharge coefficient of the weir under the investigated conditions.

To further evaluate the reliability and standing of the current findings within the broader context of hydraulic modeling, a comprehensive comparison was conducted between the present study and several recent investigations from the literature (Table 9). Table 9 summarizes the weir types, machine learning algorithms, and key recommendations from various studies focusing on discharge coefficient prediction. As tabulated, while many researchers have successfully employed algorithms such as ANN, GEP, and SVM for different weir geometries (e.g., piano-key, labyrinth, and side orifices), the current study introduces the MARS model as a highly robust alternative. The comparison reveals that although all developed models in this study (GEP, SVM, and MARS) yielded accurate results, the MARS model demonstrated superior predictive performance, consistent with the trend of continuous improvement in soft computing applications in hydraulic engineering. This comparative analysis confirms that the results obtained in this research are not only in good agreement with established literature but also offer enhanced accuracy through the application of the MARS paradigm for labyrinth and piano-key weirs.

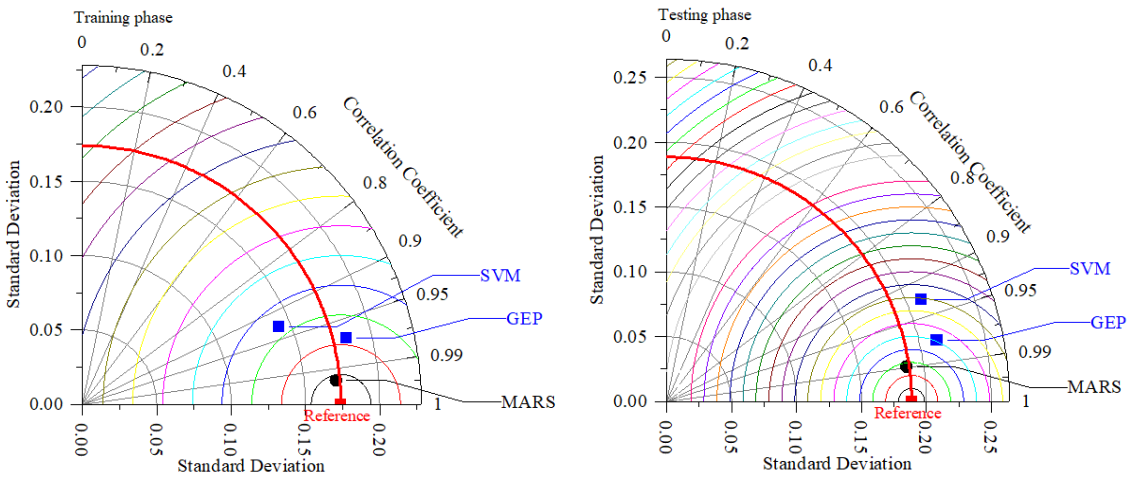


Figure 20 Models comparison using Tylor diagram

Table 9 Comparison with Previous Studies

Reference	Weir included	Models included	Recommendation
Present study	labyrinth and piano-key weirs	GEP, SVM, MARS	All models proved accurate, but MARS outperformed the others.
[15]	Labyrinth and piano-key	GEP, SVM	Both accurate; GEP showed superior performance over SVM for C_d.
[27]	Arced labyrinth weir, arced piano key weir	ANN, SVM	Both accurate; ANN outperformed SVM.
[28]	Sharp-crested triangular labyrinth weir	ANFIS, MLP, SVR, RBFNN	ANFIS-PSO achieved highest testing accuracy; MLP-FA excelled in interpolation.
[29]	Sharp-crested triangular side orifice	ANN, GEP	Both models performed well; ANN was the most reliable/accurate.
[30]	Labyrinth lateral weirs	ANN, ANFIS, SVM, GMDH, MARS	ANN and SVM showed best performance (R2=0.96), while ANFIS, MARS, and GMDH followed with slightly lower accuracy (R2=0.93-0.94)
[31]	Piano-key weir	ANN (FFBP, RBF, GRNN), ANFIS, Hybrid ANFIS (ANFIS-BBO, ANFIS-CA), Regression	Hybrid ANFIS models achieved highest accuracy; all AI models outperformed regression models;

Conclusion

This study investigated the C_d of labyrinth and piano-key weirs using experimental data obtained from a controlled hydraulic laboratory program. The experiments were conducted in a rectangular flume with dimensions of 8 m in length, 0.6 m in width, and 0.6 m in height. Several linear and arced configurations of trapezoidal, triangular, rectangular labyrinth weirs, and piano-key weirs were fabricated from Plexiglas and tested under different hydraulic conditions. Based on dimensional analysis using the Buckingham π-theorem, the governing variables were reduced to four physically meaningful dimensionless predictors, namely $\frac{H_T}{P}$, Fr, $\frac{L}{W}$ and $\frac{R}{W}$. These parameters were then used as input variables for the development of three machine-learning models: MARS, SVM, and GEP. The results demonstrated that all three models were capable of estimating C_d; however, their predictive performance differed considerably. Among the evaluated methods, the optimized MARS model provided the highest accuracy and the most stable predictions. The best MARS structure was obtained with 41 maximum basis functions, a third-order interaction degree, pruning, and a GCV error of 0.000777, indicating an effective balance between model complexity and generalization capability. The final MARS formulation consisted of 12 terms and 16 basis functions, providing a transparent mathematical representation of the nonlinear relationship between the input variables and C_d. The comparative assessment showed that MARS outperformed both SVM and GEP in the training and testing phases. In the training stage, MARS achieved RMSE=0.0194, MAE=0.0157, R^2=0.9882, and $C_{d(DDR)max}$=8.8139. In the testing stage, it maintained superior performance with RMSE=0.0266, MAE=0.0170, R^2=0.9792, and $C_{d(DDR)max}$=6.6331. These values confirm the strong predictive accuracy, low error dispersion, and high reliability of the MARS model compared with SVM and GEP. The predictor-reference analysis further revealed that $\frac{H_T}{P}$ and Fr were the dominant variables controlling the discharge coefficient, each appearing six times in the MARS basis functions. In contrast, $\frac{L}{W}$ and $\frac{R}{W}$ had secondary but meaningful roles in refining the geometric influence of the weir configuration. This confirms that hydraulic conditions primarily

govern the variation of C_d, while geometric characteristics improve the physical resolution of the model. Overall, the optimized MARS model can be considered a reliable, accurate, and interpretable data-driven tool for predicting the discharge coefficient of labyrinth and piano-key weirs. Its white-box structure, strong statistical performance, and ability to capture nonlinear interactions make it particularly suitable for hydraulic design and performance assessment of complex non-linear weir systems.

Conflict of Interest

The authors declare that they have no conflict of interest.

Author Contributions

All authors contributed equally to the preparation and development of the manuscript.

References

1. Langohr, P., Bung, D.B. and Crookston, B.M. Numerical Investigation on Energy Dissipation Processes Downstream of Labyrinth Weirs. Journal of Hydraulic Engineering. 2026;152(3): 04026003. https://doi.org/10.1061/JHEND8.HYENG-1393
2. Erpicum, S., Tullis, B.P., Lodomez, M., Archambeau, P., Dewals, B.J. and Pirotton, M. Scale effects in physical piano key weirs models. Journal of Hydraulic Research. 2016;54(6): 692-698. https://doi.org/10.1080/00221686.2016.1211562
3. Tullis, B.P., Crookston, B.M. and Young, N. Scale effects in free-flow nonlinear weir head-discharge relationships. Journal of Hydraulic Engineering. 2020;146(2): 04019056. https://doi.org/10.1061/(ASCE)HY.1943-7900.00016
4. Amir, M., Ansari, M.A., Hussain, A. and Kumar, S. ANN-based prediction of discharge coefficient in rectangular labyrinth side weirs. Discover Fluid Mechanics. 2026;2(1): 3. https://doi.org/10.1007/s44369-026-00007-5
5. Leite Ribeiro, M., Bieri, M., Boillat, J.L., Schleiss, A.J., Singhal, G. and Sharma, N. Discharge capacity of piano key weirs. Journal of Hydraulic engineering. 2012;138(2):199-203. https://doi.org/10.1061/(ASCE)HY.1943-7900.0000490
6. Anderson, R.M. and Tullis, B.P. Comparison of piano key and rectangular labyrinth weir hydraulics. Journal of Hydraulic Engineering. 2012;138(4): 358-361. https://doi.org/10.1061/(ASCE)HY.1943-7900.0000509
7. Crookston, B.M., Erpicum, S., Tullis, B.P. and Laugier, F. Hydraulics of labyrinth and piano key weirs: 100 years of prototype structures, advancements, and future research needs. Journal of Hydraulic Engineering. 2019;145(12): 02519004. https://doi.org/10.1061/(ASCE)HY.1943-7900.0001646
8. Sinha, P.K., Kumar, B. and Ahmad, Z. Experimental Study on Piano Key Weirs of an Ogee Outlet Key for Enhancement in Discharge Capacity. Journal of Irrigation and Drainage Engineering. 2026;152(4): 04026010. https://doi.org/10.1061/JIDEDH.IRENG-1069
9. Mirzad, M. and Kouchakzadeh, S. Physical and Numerical Analysis of Outflow Discharge from Type-A Piano Key Weirs Under Steady and Unsteady Flow Conditions. Water. 2026;18(2):173. https://doi.org/10.3390/w18020173
10. Quamar, M.S. and Ahmad, Z. Application of machine learning models for predicting the coefficient of discharge of Type-A Piano Key Weirs. Modeling Earth Systems and Environment. 2026;12(1): 71. https://doi.org/10.1007/s40808-025-02711-6
11. Belay, B.S. and Oertel, M. Void fraction distribution downstream of nonlinear weirs: An experimental investigation using trapezoidal A-type piano key weirs, a labyrinth weir, and a linear weir. Journal of Hydraulic Engineering. 2025;151(3): 04025006. https://doi.org/10.1061/JHEND8.HYENG-14118
12. Hamidinia, M., Heidarnejad, M., Purmohammadi, M.H. and Masjedi, A.

Effect of Stepped Sidewalls on the Performance of Trapezoidal Labyrinth Weirs and Piano Key Weirs: An Experimental Study. Journal of The Institution of Engineers (India): Series A. 2025;106(2): 605-614. https://doi.org/10.1007/s40030-025-00882-0

13. Hussein, N.S. Evaluating the Hydraulic Efficiency of Rectangular, Labyrinth, and Piano Key Weirs Under Different Factors. Mathematical Modelling of Engineering Problems. 2025;12(11). DOI: 10.18280/mmep.121128
14. Eltarabily, M.G., Kamal Hamed, A., Elkiki, M. and Selim, T. Hydraulic assessment of different types of piano key weirs. ISH Journal of Hydraulic Engineering. 2025;31(1): 8-31. https://doi.org/10.1080/09715010.2024.2415938
15. Majedi-Asl, M., Fuladipanah, M., Arun, V. and Tripathi, R.P. Using data mining methods to improve discharge coefficient prediction in Piano Key and Labyrinth weirs. Water supply. 2022;22(2): 1964-1982. https://doi.org/10.2166/ws.2021.304
16. Singh, D. and Kumar, M. Hydraulic design and analysis of piano key weirs: a review. Arabian Journal for Science and Engineering. 2022;47(4): 5093-5107. https://doi.org/10.1007/s13369-021-06370-4
17. Cortes, C. and Vapnik, V. Support-vector networks. Machine Learning. 1995;20: 273-297. https://doi.org/10.1007/BF00994018
18. Roushangar, K., Abbaszadeh, H., Saadatjoo, R. and Panahi, A. Prediction of air concentration in stepped spillways using data-oriented methods. Environment and Water Engineering. 2024;11(3): 316-325. 10.22034/ewe.2024.433409.1905
19. Fuladipanah, M., Shahhosseini, A., Rathnayake, N., Azamathulla, H.M., Rathnayake, U., Meddage, D.P.P. and Tota-Maharaj, K. In-depth simulation of rainfall–runoff relationships using machine learning methods. Water Practice & Technology. 2024;19(6): 2442-2459. https://doi.org/10.2166/wpt.2024.147
20. Fuladipanah, M., Majedi Asl, M. and Haghgooyi, A. Application of intelligent algorithm to model head-discharge relationship for submerged labyrinth and linear weirs. Journal of Hydraulics. 2020;15(2): 149-164. 10.30482/jhyd.2020.232388.1461
21. Ferreira, C. Algorithm for solving gene expression programming: a new adaptive problem. Complex Systems. 2001; 13(2): 87-129. https://doi.org/10.48550/arXiv.cs/0102027
22. Fuladipanah, M., and Majedi-Asl, M. Soft Computing Application to Amplify Discharge Coefficient Prediction in Side Rectangular Weirs. Irrigation and Water Engineering. 2022;12(4): 213-233. doi: 10.22125/iwe.2022.150692
23. Friedman, J.H. Multivariate adaptive regression splines. The annals of statistics. 1991;19(1): 1-67. DOI: 10.1214/aos/1176347963
24. Haghiabi, A., Parsaie, A. and Shamsi, Z. Intelligent Mathematical Modeling of Discharge Coefficient of Nonlinear Weirs with Triangular Plan. AUT Journal of Civil Engineering. 2019;3(2): 149-156. DOI: 10.22060/ajce.2018.14833.5500
25. Kisi, O., Azamathulla, H. M., Cevat, F., Kulls, C., Kuhdaragh, M., and Fuladipanah, M. Enhancing River flow predictions: comparative analysis of machine learning approaches in modeling stage-discharge relationship. Results Eng. 2024;22(2024): 102017. https://doi.org/10.1016/j.rineng.2024.102017
26. Noori, R., Khakpour, A., Omidvar, B., and Farokhnia, A. Comparison of ANN and principal component analysis-multivariate linear regression models for predicting the river flow based on developed discrepancy ratio statistic. Expert systems with applications. 2010;37(8): 5856-5862. 10.1016/j.eswa.2010.02.020
27. Kougdaragh, M., Omidpour, T., MajediAsl, M., Masoumpour, R., & Ayami Lord, M. (2023). Comparison of Discharge Coefficient of Arced labyrinth Weir and Arced Piano Key Weir Using Artificial Intelligence Methods. Hydrophysics, 9(1), 147-161. 20.1001.1.24767131.1402.9.1.12.7
28. Mahmoud, A., Yuan, X., Kheimi, M., & Yuan, Y. (2021). Interpolation accuracy of hybrid soft computing techniques in estimating discharge capacity of triangular

labyrinth weir. IEEE Access, 9, 6769-6785. 10.1109/ACCESS.2021.3049223.
29. Elshaarawy, M. K., & Hamed, A. K. (2024). Predicting discharge coefficient of triangular side orifice using ANN and GEP models. Water Science, 38(1), 1-20. https://doi.org/10.1080/23570008.2023.2290301
30. Parsaie, A. and Haghiabi, A.H. (2017). Improving modelling of discharge coefficient of triangular labyrinth lateral weirs using SVM, GMDH and MARS techniques. Irrigation and drainage, 66(4): 636-654. https://doi.org/10.1002/ird.2125
31. Alam, J., Muzzammil, M., & Raza, M. A. (2025). Prediction of coefficient of discharge (CPK) of A-type piano key weir using ANN and hybrid ANFIS models. Modeling Earth Systems and Environment, 11(3), 224. https://doi.org/10.1007/s40808-025-02400-4

© 2026 by the authors. Licensee SCU, Ahvaz, Iran. This article is an open access article distributed under the terms and conditions of the Creative Commons Attribution 4.0 International (CC BY 4.0 license) (http://creativecommons.org/licenses/by/4.0/).